Nano Research
2022, 15(5): 4091–4099

ISSN 1998-0124 CN 11-5974/O4
https://doi.org/10.1007/s12274-021-4035-2

Research Article

Stabilizing effects of atomic Ti doping on high-voltage high-nickel layered oxide cathode for lithium-ion rechargeable batteries

Yong Cheng[1,2,§], Yan Sun[3,§], Changting Chu[1], Limin Chang[1] (✉), Zhaomin Wang[3], Dongyu Zhang[2], Wanqiang Liu[3] (✉), Zechao Zhuang[4] (✉), and Limin Wang[1,2]

[1] *Key Laboratory of Preparation and Applications of Environmental Friendly Materials (Ministry of Education), Jilin Normal University, Changchun 130103, China*
[2] *State Key Laboratory of Rare Earth Resource Utilization, Changchun Institute of Applied Chemistry, Chinese Academy of Sciences, Changchun 130022, China*
[3] *School of materials science and engineering, Changchun University of Science and Technology, Changchun 130022, China*
[4] *Department of Chemistry, Tsinghua University, Beijing 100084, China*
[§] *Yong Cheng and Yan Sun contributed equally to this work.*

Received: 3 November 2021 / **Revised:** 29 November 2021 / **Accepted:** 30 November 2021

ABSTRACT

High-voltage high-nickel lithium layered oxide cathodes show great application prospects to meet the ever-increasing demand for further improvement of the energy density of rechargeable lithium-ion batteries (LIBs) mainly due to their high output capacity. However, severe bulk structural degradation and undesired electrode–electrolyte interface reactions seriously endanger the cycle life and safety of the battery. Here, 2 mol% Ti atom is used as modified material doping into $LiNi_{0.6}Co_{0.2}Mn_{0.2}O_2$ (NCM) to reform $LiNi_{0.6}Co_{0.2}Mn_{0.18}Ti_{0.02}O_2$ (NCM-Ti) and address the long-standing inherent problem. At a high cut-off voltage of 4.5 V, NCM-Ti delivers a higher capacity retention ratio (91.8% vs. 82.9%) after 150 cycles and a superior rate capacity (118 vs. 105 mAh·g^{-1}) at the high current density of 10 C than the pristine NCM. The designed high-voltage full battery with graphite as anode and NCM-Ti as cathode also exhibits high energy density (240 Wh·kg^{-1}) and excellent electrochemical performance. The superior electrochemical behavior can be attributed to the improved stability of the bulk structure and the electrode–electrolyte interface owing to the strong Ti–O bond and no unpaired electrons. The *in-situ* X-ray diffraction analysis demonstrates that Ti-doping inhibits the undesired H2-H3 phase transition, minimizing the mechanical degradation. The *ex-situ* TEM and X-ray photoelectron spectroscopy reveal that Ti-doping suppresses the release of interfacial oxygen, reducing undesired interfacial reactions. This work provides a valuable strategic guideline for the application of high-voltage high-nickel cathodes in LIBs.

KEYWORDS

lithium-ion battery, high-voltage high-nickel cathode, Ti-doping, structural stability, interface stability

1 Introduction

Research on secondary rechargeable batteries is an important strategy to solve current energy problems [1–4]. Lithium-ion batteries (LIBs) have been widely applied in portable electronic equipment, electric vehicles, and large-scale energy storage [5, 6]. However, their current energy density, cycle life, and safety performance are unable to meet the needs of social development, which is mainly due to the relatively low output capacity and poor cycle stability of the widely used commercial cathode materials [7, 8]. Therefore, the cathode material has become the bottleneck restricting the development of LIBs. Currently, the widely used cathode materials are the high-nickel lithium layered oxide cathodes ($LiNi_xCo_yMn_{1-x-y}O_2$, $x \geq 0.6$) [9, 10], which have relatively high specific capacities in comparison with $LiFePO_4$, $LiMn_2O_4$, $LiNi_{0.5}Mn_{1.5}O_4$, and $LiCoO_2$ cathodes [11, 12]. To further obtain higher energy density, increasing the charge cut-off voltage is becoming an effective strategy [13]. However, high voltage means the extraction of more lithium ions from the layered structure by deepening the redox reaction of transition metal, thereby increasing the specific capacity of the material. The deep electron transfer and lithium ions deintercalation will be a great challenge for the long-cycle stability of the battery [14, 15].

The deepening damage caused by high voltage can be reflected in the stability of the bulk structure and the electrode–electrolyte interface [16]. For the bulk structure, high voltage means excessive lithium ions deintercalation (*c*-axis change) and redox reaction of transition metal (*a*-axis and *b*-axis change), which lead to greater volume change and undesired harmful phase transition (H2-H3), finally exacerbating the instability of the layered structure during continuous charge and discharge cycles [17, 18]. The resulting anisotropic internal stress will cause a large number of intergranular cracks in the secondary agglomerates particles, which will expose a larger crystal surface to contact with the electrolyte and thus aggravate the problems of surface phase change and oxygen release [19, 20]. Besides, the vacancies

Address correspondence to Limin Chang, lmchang@jlnu.edu.cn; Wanqiang Liu, wqliu1979@126.com; Zechao Zhuang, zhuangzc@mail.tsinghua.edu.cn

generated by the extraction of a large number of lithium ions will promote the transfer of transition metal to the lithium layer due to the similar ionic radius (Li^+: 0.76 Å and Ni^{2+}: 0.69 Å) and increased magnetic frustration and interlayer linear superexchange interactions, which causes a large amount of Li^+/Ni^{2+} mixing and local phase transition and conversely leads to a large number of intragranular cracks in the crystal lattice and continuous capacity decay [21, 22]. Then these problems will seriously damage the stability of the bulk structure of the cathode material. For the electrode–electrolyte interface, high voltage means deep redox reaction, which will produce more unstable and highly active Ni^{4+}. Ni^{4+} tends to get electrons and becomes more stable Ni^{2+}, which promotes the loss of electrons of lattice oxygen ions in the layered structure and becomes highly active oxygen molecules [23, 24]. These changes are particularly prominent in the particle surface, which will cause the occurrence of surface phase changes (*R*3*m* layered structure → *Fd*3*m* spinel-like phase → *Fm*3*m* rock-salt phase) and the release of oxygen (surface lattice oxygen loss and electrolyte decomposition), as well as increase the charge transfer resistance and the electrode–electrolyte interface membrane resistance, thereby hindering lithium ions transport [25, 26]. Besides, due to the overlap of the electronic energy levels of $Co^{3+/4+}$ and O^{2-}, it can also promote the production of oxygen when Co provides capacity under high voltage [27, 28]. In addition, the high voltage will aggravate the decomposition of carbonate solvents and lithium salts in the electrolyte and deposit them on the surface of the materials, which will cause severe polarization and interface impedance, thus causing more dead lithium and reducing capacity [29, 30]. These problems will seriously deteriorate the electrode–electrolyte interface environment and cause poor cycle stability and thermal stability. From this point of view, it is very important to develop effective modification strategies to improve the cycle stability of materials under high voltage.

Concentration gradient [31], surface coating [32], bulk doping [33], and electrolyte design [34] are the most commonly used modification methods. Among them, bulk doping modification can fundamentally affect the crystal structure and the atomic chemical environment of the material, thereby improving the lithium ions storage performance of the material from the root. The single atoms doped inside the lattice can play a dual role in physics and chemistry [35, 36]. In terms of physics, it can not only support the stable passage of the layered structure as a pillar but also inhibit the phase transition caused by the migration of transition metals due to its greater electromagnetic force [37]. In terms of chemistry, doped single atoms can often inhibit the loss of lattice oxygen atoms due to their relatively large Me–O bond energy [38]. Many dopants such as Na [39], Mg [40], Al [41], Nd [42], Zn [43], W [44], Te [45], Zr [46], and Mo [47] have been introduced into high-nickel lithium layered oxide cathodes to improve their electrochemical performance. For example, Xie et al. [40] present the 2 mol% Mg-doped $Li_{0.98}Mg_{0.02}Ni_{0.94}Co_{0.06}O_2$ cathode, which delivers high capacity retention (80.1%) after 500 cycles in full cells owing to the modification effect of Mg^{2+} which is acted as a pillar in the lithium layer to effectively suppress the undesirable coexistence of H2 and H3. Jeong et al. [41] investigate Al-doped Ni-rich $LiNi_{0.80}Co_{0.15}Mn_{0.05}O_2$ cathode, which exhibits lower polarization potential, better rate capability, and cycle stability due to the alleviation of anisotropic lattice changes and volume changes during cycling. Cui et al. [43] design the 2 mol% Zn-doped $LiNi_{0.94}Co_{0.04}Zn_{0.02}O_{1.99}$ cathode, which retains 74% of the initial capacity after 500 cycles in a full cell because Zn-doping promotes smoother phase transition, suppresses anisotropic lattice distortion, and maintains the mechanical integrity of cathode particles. Sun et al. [44] present the 2 mol% W-doped $LiNiO_2$ cathode, which reveals high capacity retention (95.5%) after 100 cycles on account of the influence of W-doping, which combines two-phase reactions (H2/H3) into a single phase. Thesestudieshaveshownthatdopingmodificationcangreatlyimprove the electrochemical performance of materials. However, for high-voltage high-nickel cathode materials, Ti dopant must attract enough attention because it has a stronger Ti–O bond and no unpaired electrons, which has obvious advantages for maintaining the stability of the layered structure and lattice oxygen.

In this work, we have successfully prepared a 2 mol% Ti-doped $LiNi_{0.6}Co_{0.2}Mn_{0.18}Ti_{0.02}O_2$ (NCM-Ti) high-nickel cathode material through a liquid phase physical mixing and high-temperature annealing method. Due to the enhanced stability of the bulk structure and the electrode–electrolyte interface after introducing Ti, NCM-Ti displays outstanding electrochemical properties in terms of cycle stability and high-rate capability at 4.5 V high voltage. In addition, the mechanism of Ti-doping has been fully elucidated by systematically comparing the properties of layered structure information, layered structure stability, lithium ions diffusion kinetics, and electrode–electrolyte interface of the pristine NCM and NCM-Ti samples. The properties of the strong Ti–O bond and no unpaired electrons of Ti play a vital role in improving the lithium ions storage performance of the high-nickel cathode material under the condition of high voltage. Therefore, the Ti element is an optimal dopant candidate in improving the performance of high-voltage and high-nickel cathode materials in LIBs.

2 Experimental section

2.1 Material preparation

$Ni_{0.6}Co_{0.2}Mn_{0.2}(OH)_2$ precursor (Fig. S1 in the Electronic Supplementary Material (ESM)) was prepared by a hydroxide coprecipitation method with the detailed process described previously [48]. Briefly, the appropriate concentration of $NiSO_4{\cdot}6H_2O$, $CoSO_4{\cdot}7H_2O$, $MnSO_4{\cdot}H_2O$, NaOH, and NH_4OH aqueous solution was continuously pumped into the continuous stirring tank reactor (CSTR). The total ammonia concentration in the reactor was 1 mol·L^{-1}. The stirring speed (1,000 rpm·min^{-1}), pH (11.7), and temperature (60 °C) were carefully controlled during the coprecipitation reaction. The obtained precursor was washed and filtered several times with distilled water, and then dried at 80 °C overnight. The pristine $LiNi_{0.6}Co_{0.2}Mn_{0.2}O_2$ (NCM) was prepared by calcining a mixed powder of $Ni_{0.6}Co_{0.2}Mn_{0.2}(OH)_2$ and $LiOH{\cdot}H_2O$ (molar ratio of (Ni + Co + Mn):Li = 1:1.05) at 850 °C for 10 h in air atmosphere. To obtain NCM-Ti, an appropriate amount of the $Ni_{0.6}Co_{0.2}Mn_{0.2}(OH)_2$ precursor was added to the nano-TiO_2 anhydrous ethanol dispersion and then stirred in a homogenizer at a speed of 3,000 rpm·min^{-1} for 5 min to obtain a viscous slurry. The dried TiO_2@$Ni_{0.6}Co_{0.2}Mn_{0.2}(OH)_2$ powder and $LiOH{\cdot}H_2O$ (molar ratio of (Ni + Co + Mn + Ti):Li = 1:1.07) were homogeneously mixed and calcined at 850 °C for 10 h in air. $LiNi_{0.6}Co_{0.2}Mn_{0.19}Ti_{0.01}O_2$ (Ti-1% NCM) and $LiNi_{0.6}Co_{0.2}Mn_{0.17}Ti_{0.03}O_2$ (Ti-3% NCM) were also prepared using the above method separately (Fig. S2 in the ESM).

2.2 Material characterization

Scanning electron microscopy (SEM, Qunta250) and FEI G2 S-Twin high-resolution transmission electron microscopy (HRTEM) characterized morphology and lattice information. Energy-dispersive X-ray spectrometer (EDS, Quantax 200) determined element distribution. X-ray photoelectron spectrometer (ESCALABMKLL) characterized the element valence. Bruker D8 Advance powder X-ray diffractometer

examined the structure information from 10° to 80° at 1°·min^{-1}. X-raydiffractometercombinedwithaNEWAREbatterytesterwasusedfor *in-situ* X-ray diffraction (XRD) measurement. The battery was tested once under the current density of 20 mA·g^{-1}. A single XRD spectrum took 12 min from 10° to 80°.

2.3 Electrochemical measurement

The electrode was prepared as follows: active material, C45, KS-6, and polyvinylidene fluoride (PVDF) with a weight ratio of 90:4.5:3:2.5 in N-methylpyrrolidone (NMP) solution were evenly stirred and cast on an Al foil with an active material loading of about 5 mg·cm^{-2}. Then they were vacuum-dried and cut into circular electrodes (diameter 12 mm). CR2025 coin cell was used to characterize the electrochemical performances of the as-prepared materials. Li foil was used as the counter electrode for the half battery. The electrolyte was 1 M $LiPF_6$ in ethyl carbonate and ethyl methyl carbonate (EC:EMC = 3:7 by volume). The commercial graphite was used as the anode material for the full battery and the negative/positive (N/P) ratio was controlled at about 1.2. The electrolyte was the above electrolyte plus 2 wt.% vinylene carbonate (VC) additive. Galvanostatic charge–discharge was tested on the NEWARE battery tester (5 V, 20 mA). BioLogic VMP3 electrochemical workstation was used to test electrochemical impedance spectroscopy (EIS) and cyclic voltammogram (CV) data. The EIS test was performed by applying an amplitude of 5 mV in the frequency range of 100 mHz to 200 kHz when fully discharged to 3.0 V at different cycles. For the galvanostatic intermittent titration technique (GITT) measurement, the result was obtained by charging and discharging the cells for 30 min at 20 mA·g^{-1} between 3 and 4.5 V followed by 120 min of relaxation time for each interval.

3 Results and discussion

3.1 Morphology and structure

The Ti-doping modification materials are successfully prepared through a simple liquid-phase mixing calcination method. The SEM and HRTEM images for the pristine NCM and NCM-Ti samples are shown in Figs. 1(a)–1(c) and Figs. 1(d)–1(f), respectively. In comparison with the pristine NCM, the morphology of NCM-Ti has not changed significantly, and it still shows a spherical agglomerate with the size of about 10 μm formed by close packing of single-crystal primary particles, and no impurities are formed and accumulated on the particle surface [49] (Fig. S3 in the ESM). The interplanar spacing of the 003 crystal plane of NCM-Ti is slightly larger than that of the pristine NCM (0.479 vs. 0.472 nm), which confirms that Ti^{4+} is indeed doped into the crystal lattice, and it can also be further proved by the following XRD data. Figure 1(g) shows the EDS elemental mapping for NCM-Ti. Ni, Co, Mn, and Ti element are all uniformly distributed in the whole particle and no element separation occurs. Figures 2(a) and 2(b) show the Rietveld refinements of XRD patterns for the pristine NCM and NCM-Ti samples. All the diffraction peaks can be indexed to a hexagonal layered structure with the R3m space group and no impurities are detected [50]. The refinement result is also shown in Table S1 in the ESM. It can be seen that the *c*-axis lattice parameter increases from 14.2244 to 14.2332 Å, which further confirms that Ti is doped into the lattice of the layered material. X-ray photoelectron spectroscopy (XPS) was also used to characterize the element valence states of the materials. Noted that the two characteristic peak positions of Ti 2p are located at 458.3 and 463.9 eV, respectively (Fig. 2(c)), indicating the valence state of Ti is indeed +4, which further demonstrates that Ti^{4+} is doped into NCM-Ti [51]. The two characteristic peaks of Ni 2p correspond well to Ni^{2+} and Ni^{3+} (Fig. 2(d)) [52]. Noted that the XPS peak of Ni 2p for NCM-Ti is deviated to the right by 0.8 eV, which is attributable to the introduction of higher valence Ti^{4+} that needs to produce more Ni^{2+} for charge compensation [53]. The XPS peaks of Co and Mn also correspond well to Co^{3+} and Mn^{4+}, respectively (Figs. 2(e) and 2(f)) [54], and no obvious peak shift can be observed for the pristine NCM and NCM-Ti samples. Based on the above analysis, it can be reasonable to conclude that Ti^{4+} has been uniformly doped into high-nickel lithium layered oxide cathode material

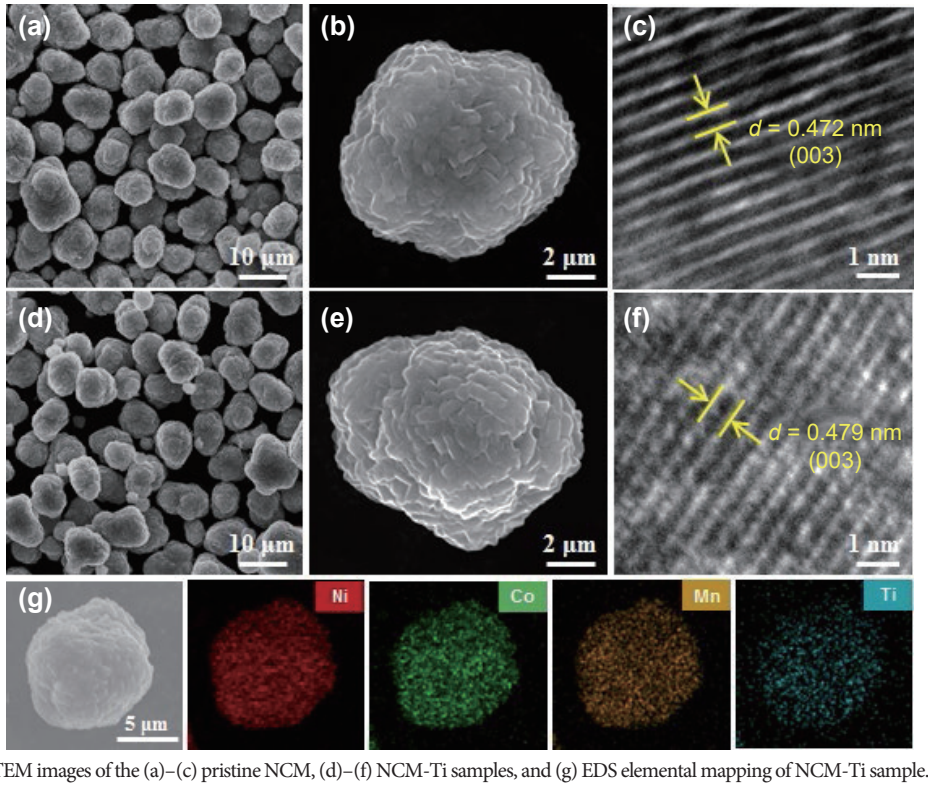

Figure 1 SEM and HRTEM images of the (a)–(c) pristine NCM, (d)–(f) NCM-Ti samples, and (g) EDS elemental mapping of NCM-Ti sample.

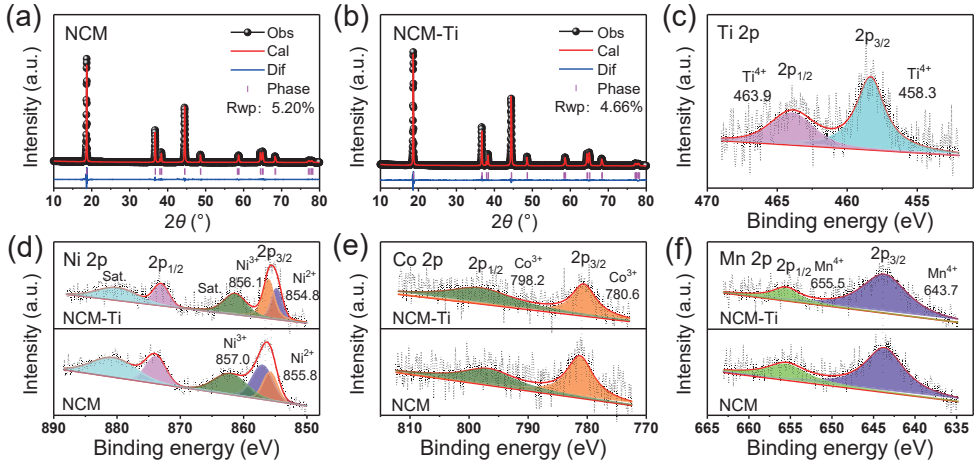

Figure 2 Rietveld refinements of XRD patterns for (a) pristine NCM and (b) NCM-Ti samples. (c) XPS data of Ti element for the NCM-Ti sample. (d)–(f) Comparison of the XPS data of Ni, Co, and Mn element for the pristine NCM and NCM-Ti samples.

with good morphology and crystal structure.

3.2 Electrochemical performance

The electrochemical performance of the pristine NCM and NCM-Ti samples were fully examined and compared to understand the impact of Ti-doping. The CV curves of the initial five cycles were firstly performed for the two samples (Figs. 3(a) and 3(b)). It can be seen that there is a pair of obvious redox peaks at 3.8/3.7 V, corresponding to the conversion reactions between $Ni^{2+/3+}$ and Ni^{4+} [42]. Another pair of unobvious redox peaks at 4.3/4.2 V is related to the conversion reactions between Co^{3+} and Co^{4+} [42]. Noted that the CV curves of NCM-Ti exhibit better reversibility compared to pristine NCM after the first anodic and cathodic scan, which signifies that Ti-doping improves the stability of the layered structure of the material. Figure 3(c) shows their initial charge–discharge curves at 0.1 C and 4.5 V high voltage. NCM-Ti delivers a specific capacity of 193 mAh·g^{-1}, which is slightly lower than that of NCM (197 mAh·g^{-1}). Figure 3(d) exhibits their cycle performances at 0.5 C. It can be seen that NCM-Ti shows a higher capacity retention ratio (91.8% vs. 82.9%) in comparison with the pristine NCM after 150 cycles. The corresponding charge–discharge curves from the 10th to the 150th cycle for the pristine NCM and NCM-Ti samples are also depicted in Figs. 3(e) and 3(f). NCM-Ti displays a smaller discharge median voltage attenuation compared to the pristine NCM. The discharge median voltage of NCM-Ti declines from 3.81 to 3.79 V (0.02 V), and that of NCM declines from 3.8 to 3.76 V (0.04 V). The long cycle performance of the NCM-Ti sample at a high current density of 1 C and high voltage of 4.5 V was also tested (Fig. 3(g)). It can be still maintained at a high specific capacity of 144 mAh·g^{-1} after 250 cycles, with a capacity retention ratio of 82.8%. Furthermore, the electrochemical performances of NCM-Ti and NCM at 4.3 V are also characterized (Fig. 3(h) and Fig. S4 in the ESM). NCM-Ti exhibits a high capacity retention

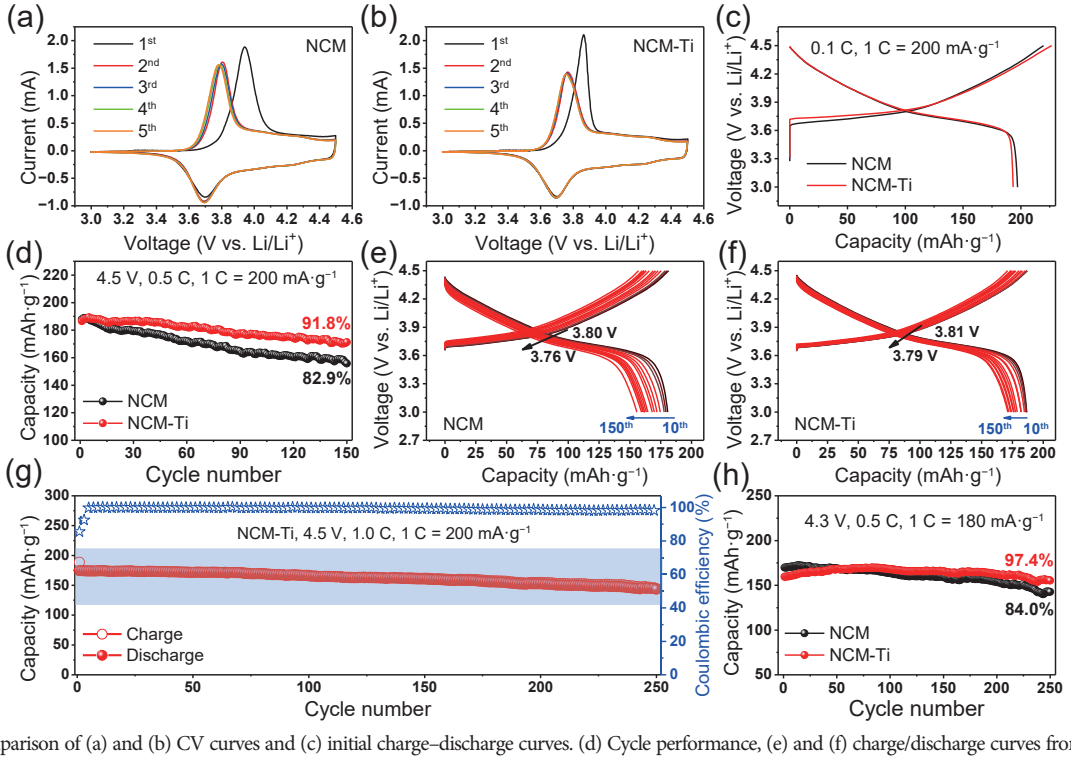

Figure 3 Comparison of (a) and (b) CV curves and (c) initial charge–discharge curves. (d) Cycle performance, (e) and (f) charge/discharge curves from the 10th cycle to 150th cycle of the pristine NCM and NCM-Ti samples under 4.5 V high voltage. (g) The long cycle performance for the NCM-Ti sample at 1 C current density and 4.5 V high voltage. (h) Comparison of long cycle performance for 4.3 V low voltage of the pristine NCM and NCM-Ti samples.

ratio of 97.4% after 250 long cycles, and the NCM-Ti sample also shows superior electrochemical performance compared to the results reported in the literature of other doping modification studies (Table S2 in the ESM). The results demonstrate that Ti-doping exhibits greatly improved cycle stability even at a high voltage of 4.5 V, which fully confirms that Ti-doping plays a significant role in stabilizing the bulk layered structure and the electrode–electrolyte interface, thereby enhancing the overall performance of the battery.

3.3 Bulk structure stability

To further evaluate the effect of Ti-doping on the layered structure and phase transition, *in-situ* XRD characterization is also performed for the pristine NCM and NCM-Ti samples. Figures 4(a) and 4(b) show the contour plot and detailed exhibition of the (003) and (101) peaks and the corresponding voltage–capacity curves for both samples. They all show a similar structural evolution process to the previous research [55–57]: the (003) peak initially shifts toward a lower 2θ angle, implying an increase in the *c*-axis, which is due to the increasing electrostatic repulsion between the oxygen anions at adjacent layers after partial extraction of lithium ions. The process corresponds to the transition from H1 to H2 phase. Then the (003) peak sharply shifted toward a higher 2θ angle, suggesting the steep shrinkage of the *c*-axis, which is owing to that the gravity effect is greater than the electrostatic repulsion after lithium ions were largely extracted. The process corresponds to the transition from H2 to H3 phase. Noted that the *c*-axis shrinkage process (H2 to H3) is more rapid and aggressive than the initial *c*-axis expansion (H1 to H2), which will lead to a serious accumulation of internal strain and destroy the structural stability of the material. In addition, the (101) peak continues to turn to a higher 2θ angle during the whole charging process, implying the shrinkage of the *a*-axis and *b*-axis, which was due to the oxidation of transition metal ions, leading to a smaller ion radius. However, it is easy to see that there are still some differences between the two samples. For the H2 to the H3 phase transition process, noted that the pristine NCM turned to a higher angle compared to NCM-Ti, which implies that the pristine NCM has a greater degree of *c*-axis shrinkage and a stronger H2 to H3 phase transition [58]. It also signifies that the pristine NCM sample will suffer severe volume change and capacity loss. However, Ti-doping can well suppress such damage behavior, thereby minimizing the structure degradation. The reason can be attributed to the strong Ti–O bond, forming a stronger layered structure frame, which has a shielding effect on the violent expansion and contraction behavior of the layered structure. Then it will effectively suppress the formation of undesirable H3 phase and stabilize the layered structure. The particle morphologies of the pristine NCM and NCM-Ti samples after 100 cycles are also shown in Figs. 4(c) and 4(d). Noted that there is a microcrack in the pristine NCM sample, while the structure of the NCM-Ti sample is intact, which is corresponded well to the harm caused by the more intense transition from H2 to H3 phase. The refined XRD patterns of the pristine NCM and NCM-Ti samples after 100 cycles were also carried out (Figs. 4(e) and 4(f)). They both still maintain a well-layered structure. However, the pristine NCM delivered a higher degree of Li^+/Ni^{2+} mixing compared to NCM-Ti (4.71% vs. 3.32%), which indicates that Ti-doping can effectively suppress the Li^+/Ni^{2+} mixing. This phenomenon can be attributed to the fact that Ti^{4+} has no

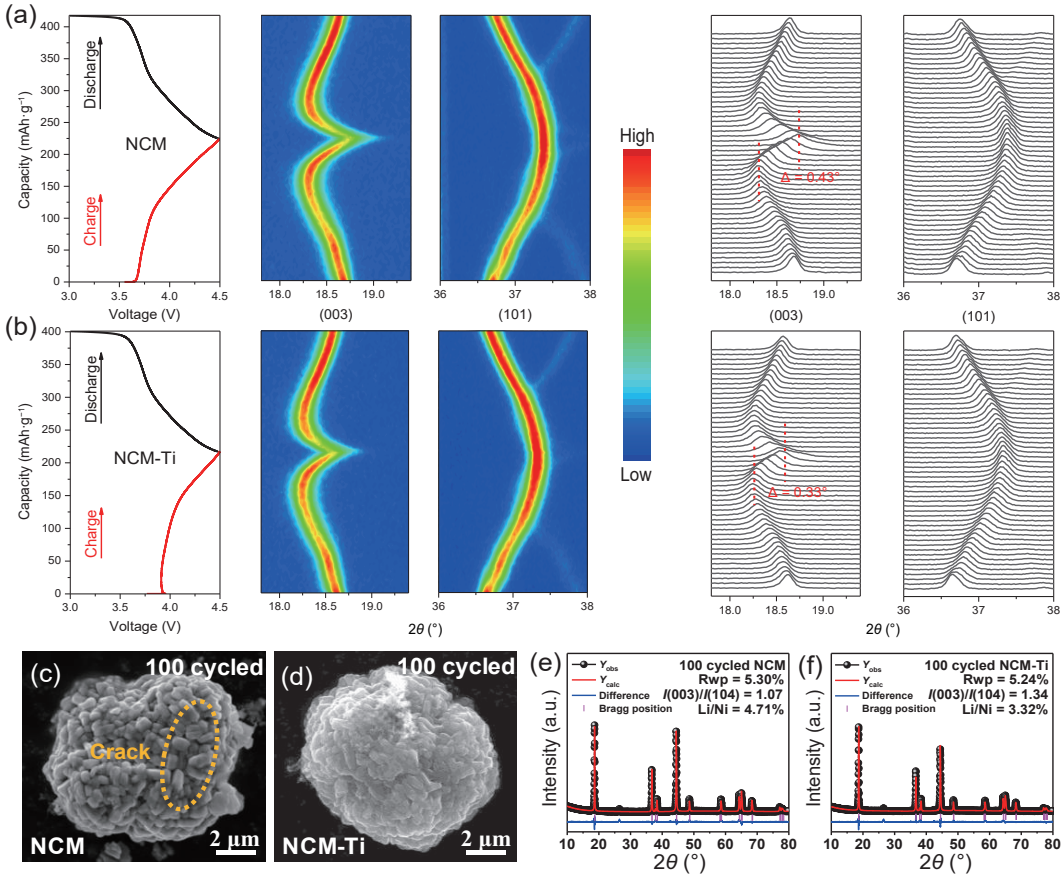

Figure 4 Comparison of (a) and (b) *in-situ* XRD data during the first charge and discharge process: the profile of the (003) and (101) peaks diffraction patterns with the corresponding voltage–capacity curve. (c) and (d) SEM images after 100 cycles, (e) and (f) refined XRD patterns after 100 cycles for the pristine NCM and NCM-Ti samples.

unpaired electrons in the outer orbital, which can screen the 180° Ni^{2+}–O^{2-}–Ni^{2+} interlayer linear superexchange interactions and relieve magnetic frustration, thereby reducing the Li^+/Ni^{2+} disordering [59, 60]. Then it will be conducive to maintaining the stability of the layered structure and improving the diffusion kinetics of lithium ions.

Rate performance of NCM and NCM-Ti are also shown in Fig. 5(a) and Fig. S5 in the ESM. It can be seen that NCM-Ti can deliver a higher rate capacity (118 vs. 105 mAh·g^{-1}) at 10 C than that of the pristine NCM. GITT measurement was used to evaluate the effect of Ti-doping on lithium ions diffusion kinetics (Fig. S6 in the ESM). Figure 5(b) shows the calculated actual lithium ions diffusion coefficients (D_{Li}^+) at different voltages for the pristine NCM and NCM-Ti samples. It can be seen that D_{Li}^+ of NCM-Ti is about $10^{-8.4}$ cm^2·s^{-1}, which is higher than the average D_{Li}^+ value of NCM ($10^{-8.8}$ cm^2·s^{-1}). CV measurements at different scan rates were also performed to qualitatively compare the lithium ions diffusion capabilities of the pristine NCM and NCM-Ti samples (Fig. 5(c) and Fig. S7 in the ESM). The apparent D_{Li}^+ was analyzed through the Randles–Sevcik equation [61].

$$\mathrm{Ip} = (2.68 \times 10^5) n^{3/2} A D^{1/2} C \omega^{1/2} \qquad K = (2.68 \times 10^5) n^{3/2} A D^{1/2} C$$

where the n (number of electron transfers), A (electrode area), and C (lithium ions molar concentration) are the relatively consistent values for NCM and NCM-Ti samples. The plot of oxidation/reduction peak current (Ip) and the square root of the scan rate ($\omega^{1/2}$) is shown in Fig. 5(d), which both show a linear relationship. It can be inferred that the slope is proportional to the apparent D_{Li}^+, the larger the slope, the faster the lithium ions diffusion rate [61]. Then we can see that NCM-Ti exhibits a larger slope than the pristine NCM, which further indicates that Ti-doping enhances the lithium ions diffusion kinetics during the charge and discharge process. This improved lithium diffusion kinetics is not only due to the maintenance of the bulk layered structure, but also depends on the improvement of the electrode–electrolyte interface environment.

3.4 Electrode–electrolyte interface stability

The electrode–electrolyte interface stability under high voltage also greatly affects the cell performance and is related to the stability of the bulk structure of the cathode material. For example, more highly active and unstable Ni^{4+} will be generated on the surface of the material at high voltage, which will encourage it to capture the electrons of oxygen atoms and spontaneously transform to more stable Ni^{2+}. Then a more serious surface phase transition will occur (layered → spinel → rock salt phase), which can hinder the deintercalation of active lithium ions and increase the interface resistance [19]. Meanwhile, more active oxygen on the material surface will be generated and released into the electrolyte due to the loss of electrons for oxygen ions, which will aggravate the decomposition of the electrolyte [26]. The secondary particles will produce more micro-cracks due to the existence of anisotropic internal stress during the continuous charge and discharge process, which will further increase the contact area between the material and the electrolyte, thereby intensifying the above-mentioned adverse reactions [62]. Therefore, the improvement of the bulk structure stability will also help to improve the electrode–electrolyte interface stability.

Figure 5(e) shows their overall polarization voltage for different cycles. It can be seen that NCM-Ti exhibits a smaller polarization voltage compared to the pristine NCM, which further confirms that Ti-doping effectively suppresses the undesired interfacial reactions on the electrode–electrolyte surface. Figure S8 in the ESM exhibits their 1st, 10th, and 100th electrochemical impedance spectra after two activations. For the EIS [52], the first semicircle (high-middle frequency region) corresponds to the interface film resistance, which is derived from the cathode electrolyte interface (CEI) film. The second semicircle (middle-low frequency region) is related to the interface charge transfer resistance of the cathode material (R_{ct}). The diameter of the semicircle corresponds to the

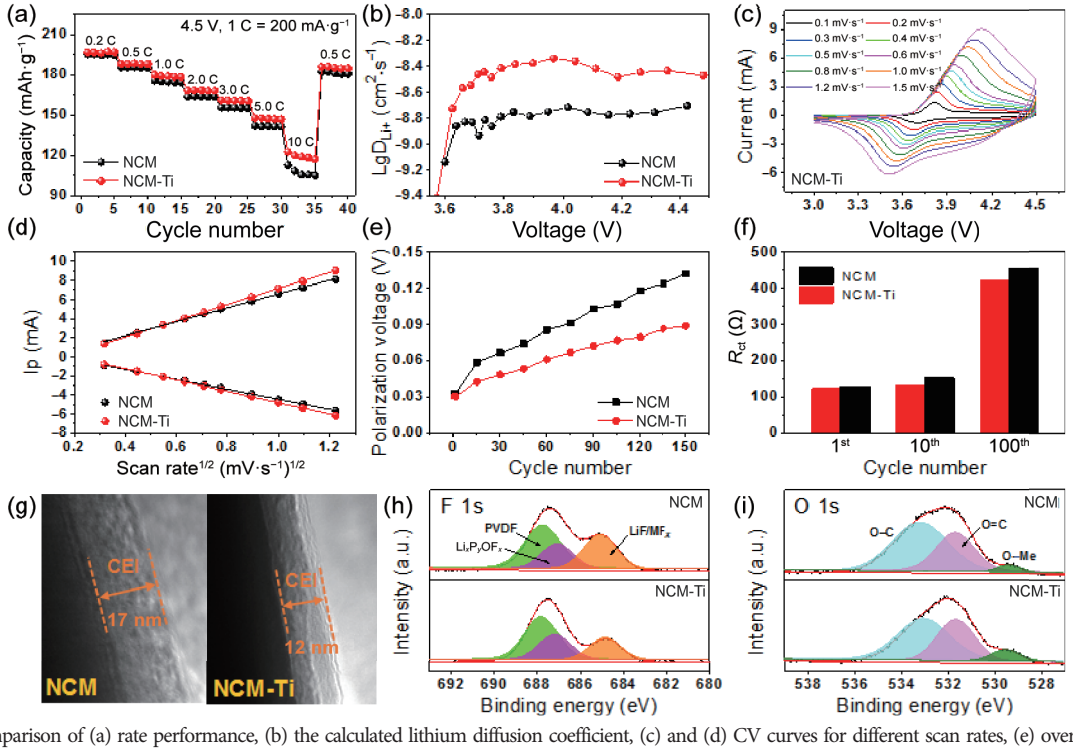

Figure 5 Comparison of (a) rate performance, (b) the calculated lithium diffusion coefficient, (c) and (d) CV curves for different scan rates, (e) overall polarization voltage, (f) fitted electrochemical impedance values of different cycles, (g) the CEI film of the samples after 100 cycles, (h) F 1s spectra, and (i) O 1s spectra XPS data after 100 cycles for the pristine NCM and NCM-Ti samples.

resistance value. The impedance fitting results can be seen in Fig. 5(f). The R_{ct} values of NCM-Ti are smaller than those of the pristine NCM, which is due to the small amount of undesirable electrode–electrolyte interface reactions and surface phase transition. Fig. 5(g) shows the thickness of the CEI film of the pristine NCM and NCM-Ti samples after 100 cycles. Noted that the CEI film of NCM-Ti is thinner than that of the pristine NCM (12 vs. 17 nm), which indicates that the decomposition of the electrolyte is effectively suppressed. XPS is also used to check the surface chemistry differences of the pristine NCM and NCM-Ti samples after 100 cycles. Noted that the LiF/MF_x peak for the NCM-Ti sample is weaker (Fig. 5(h)), signifying the less electrolyte decomposition and transition metal dissolution. The O–Me peak of the NCM-Ti sample is also stronger (Fig. 5(i)), implying less oxygen loss after Ti-doping. The above results prove that the Ti-doping modification indeed increases the stability of the electrode–electrolyte interface, which also further demonstrates the beneficial effect of Ti-doping in improving structural stability.

3.5 Electrochemical performances of full-battery

The superior electrochemical performance of the NCM-Ti sample has also been further confirmed by using a high-voltage lithium full battery with commercial graphite as the anode (Fig. 6(a)). The capacity balance between negative and positive is controlled at about 1.2 (i.e., N/P = 1.2), which is achieved by adjusting the active material load of the electrode. According to the constructed capacity balance relationship, the voltage range of the full battery can be determined between 2.75–4.45 V. Figure 6(b) shows the initial charge and discharge curve. Figure 6(c) exhibits the cycle stability performance at 0.5 C, and the full battery (NCM-Ti || graphite) has a capacity retention ratio of 92.1% after 100 cycles. The rate performance is also characterized in Fig. 6(d) and Fig. S9 in the ESM. It can deliver a high specific capacity of 137 mAh·g^{-1} at 5 C. The energy density of the full battery was also calculated by the model formula [54] shown in Fig. 6(e). It is noted that it can reach 240 Wh·kg^{-1} for the NCM-Ti || graphite full battery. These results indicate that Ti-doping modified high-voltage high-nickel cathode materials have great potential in the pursuit of high-energy-density LIB applications.

4 Conclusions

In summary, we have successfully prepared a 2 mol% Ti-doped high-nickel cathode NCM-Ti through a liquid phase physical mixing and high-temperature annealing method. The homogeneous Ti-doping was achieved without triggering impurity accumulation on the agglomerate surface. NCM-Ti delivers a higher capacity retention ratio (91.8% vs. 82.9%) after 150 cycles and a superior rate capacity (118 vs. 105 mAh·g^{-1}) at 10 C than the pristine NCM under 4.5 V high voltage. For the designed NCM-Ti || graphite full battery, the capacity retention ratio is as high as 92.1% after 100 cycles and the energy density is up to 240 Wh·kg^{-1}. The superior electrochemical performance can be attributed to the improvement of the layer structure stability, lithium ions diffusion kinetics and electrode–electrolyte interface stability of the material under high voltage by Ti-doping. The *in-situ* XRD demonstrates that Ti-doping inhibits the undesired H2-H3 phase transition, minimizing the mechanical degradation. The reason can be attributed to the strong Ti–O bond forming a stronger layered structure frame, which has a shielding effect on the violent expansion and contraction behavior of the layered structure. *Ex-situ* SEM and XRD characterizations confirm that Ti-doping suppresses particle crushing and cation mixing. *Ex-situ* EIS, TEM, and XPS characterization show that Ti-doping can effectively inhibit side reactions on the electrode–electrolyte interface. The properties of the strong Ti–O bond and no unpaired electrons of Ti element play an active role in improving the stability of bulk structure and the electrode–electrolyte interface for the high-voltage high-nickel cathode materials. We suggest that the Ti element should be a preferred dopant candidate in improving the performance of high-voltage high-nickel cathode materials in LIBs.

Acknowledgements

This work is financially supported by the National Key R&D Program of China (No. 2017YFE0198100), the National Natural Science Foundation of China (Nos. 21975250 and 52072145), the Beijing Natural Science Foundation (No. 2214061), the Scientific and Technological Developing Project of Jilin Province, China (No. YDZJ202101ZYTS185), the Capital Construction Fund Projects within the Budget of Jilin Province, China (No. 2021C037-2), the Open Project Program of Key Laboratory of Preparation and Application of Environmental Friendly Materials (Jilin Normal University), Ministry of Education, China (No. 2020005), and the Open Program of State Key Laboratory of Metastable Materials Science and Technology (Yanshan University), China (No. 202110).

Electronic Supplementary Material: Supplementary material (XRD Rietveld refinements result, comparison of electrochemical performance with related literature, cycle and rate performance of materials with different doping quantities, electrochemical performance of NCM-Ti samples at 4.3 V low voltage, GITT

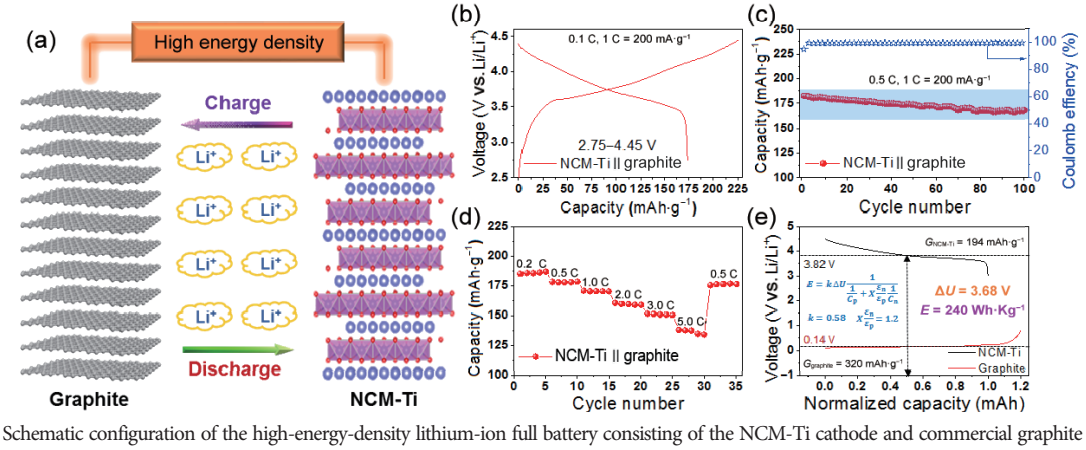

Figure 6 (a) Schematic configuration of the high-energy-density lithium-ion full battery consisting of the NCM-Ti cathode and commercial graphite anode. (b) The initial charge–discharge curves, (c) cycle performance, and (d) rate performance of the designed lithium-ion full battery. (e) Calculation of energy density for the full battery, where the k value in the empirical model was supposed as 0.58.

curves, CV curves of different scan rates, and EIS test) is available in the online version of this article at https://doi.org/10.1007/s12274-021-4035-2.

References

[1] Ma, L. B.; Lv, Y. H.; Wu, J. X.; Xia, C.; Kang, Q.; Zhang, Y. Z.; Liang, H. F.; Jin, Z. Recent advances in anode materials for potassium-ion batteries: A review. *Nano Res.* **2021**, *14*, 4442–4470.

[2] Chen, Y.; Kang, Q.; Jiang, P. K.; Huang, X. Y. Rapid, high-efficient and scalable exfoliation of high-quality boron nitride nanosheets and their application in lithium-sulfur batteries. *Nano Res.* **2021**, *14*, 2424–2431.

[3] Zhao, J.; Zhang, Y. Z.; Chen, J. Y.; Zhang, W. L.; Yuan, D.; Chua, R.; Alshareef, H. N.; Ma, Y. W. Codoped holey graphene aerogel by selective etching for high-performance sodium-ion storage. *Adv. Energy Mater.* **2020**, *10*, 2000099.

[4] Liang, J.; Zhu, G. Y.; Zhang, Y. Z.; Liang, H. F.; Huang, W. Conversion of hydroxide into carbon-coated phosphide using plasma for sodium ion batteries. *Nano Res.*, in press, https://doi.org/10.1007/s12274-021-3738-8.

[5] Dunn, B.; Kamath, H.; Tarascon, J. M. Electrical energy storage for the grid: A battery of choices. *Science* **2011**, *334*, 928–935.

[6] Armand, M.; Tarascon, J. M. Building better batteries. *Nature* **2008**, *451*, 652–657.

[7] Manthiram, A. A reflection on lithium-ion battery cathode chemistry. *Nat. Commun.* **2020**, *11*, 1550.

[8] Jiang, K. Z.; Guo, S. H.; Pang, W. K.; Zhang, X. P.; Fang, T. C.; Wang, S. F.; Wang, F. W.; Zhang, X. Y.; He. P.; Zhou, H. S. Oxygen vacancy promising highly reversible phase transition in layered cathodes for sodium-ion batteries. *Nano Res.* **2021**, *14*, 4100–4106.

[9] Wu, K.; Li, Q.; Dang, R. B.; Deng, X.; Chen, M. M.; Lee, Y. L.; Xiao, X. L.; Hu, Z. B. A novel synthesis strategy to improve cycle stability of $LiNi_{0.8}Mn_{0.1}Co_{0.1}O_2$ at high cut-off voltages through core-shell structuring. *Nano Res.* **2019**, *12*, 2460–2467.

[10] Lai, Y. J.; Li, Z. J.; Zhao, W. X.; Cheng, X. N.; Xu, S.; Yu, X.; Liu, Y. An ultrasound-triggered cation chelation and reassembly route to one-dimensional Ni-rich cathode material enabling fast charging and stable cycling of Li-ion batteries. *Nano Res.* **2020**, *13*, 3347–3357.

[11] Li, W. D.; Erickson, E. M.; Manthiram, A. High-nickel layered oxide cathodes for lithium-based automotive batteries. *Nat. Energy* **2020**, *5*, 26–34.

[12] Xu, G. L.; Liu, X.; Daali, A.; Amine, R.; Chen, Z. H.; Amine, K. Challenges and strategies to advance high-energy nickel-rich layered lithium transition metal oxide cathodes for harsh operation. *Adv. Funct. Mater.* **2020**, *30*, 2004748.

[13] Li, W. D.; Song, B. H.; Manthiram, A. High-voltage positive electrode materials for lithium-ion batteries. *Chem. Soc. Rev.* **2017**, *46*, 3006–3059.

[14] Zhang, S.; Ma, J.; Hu, Z. L.; Cui, G. L.; Chen, L. Q. Identifying and addressing critical challenges of high-voltage layered ternary oxide cathode materials. *Chem. Mater.* **2019**, *31*, 6033–6065.

[15] Yang, L. Y.; Yang, K.; Zheng, J. X.; Xu, K.; Amine, K.; Pan, F. Harnessing the surface structure to enable high-performance cathode materials for lithium-ion batteries. *Chem. Soc. Rev.* **2020**, *49*, 4667–4680.

[16] Tian, C. X.; Lin, F.; Doeff, M. M. Electrochemical characteristics of layered transition metal oxide cathode materials for lithium ion batteries: Surface, bulk behavior, and thermal properties. *Acc. Chem. Res.* **2018**, *51*, 89–96.

[17] Romano Brandt, L.; Marie, J. J.; Moxham, T.; Förstermann, D. P.; Salvati, E.; Besnard, C.; Papadaki, C.; Wang, Z. F.; Bruce, P. G.; Korsunsky, A. M. Synchrotron X-ray quantitative evaluation of transient deformation and damage phenomena in a single nickel-rich cathode particle. *Energy Environ. Sci.* **2020**, *13*, 3556–3566.

[18] Cheng, X. P.; Li, Y. H.; Cao, T. C.; Wu, R.; Wang, M. M.; Liu, H.; Liu, X. Q.; Lu, J. X.; Zhang, Y. F. Real-time observation of chemomechanical breakdown in a layered nickel-rich oxide cathode realized by *in situ* scanning electron microscopy. *ACS Energy Lett.* **2021**, *6*, 1703–1710.

[19] Hwang, S.; Chang, W.; Kim, S. M.; Su, D.; Kim, D. H.; Lee, J. Y.; Chung, K. Y.; Stach, E. A. Investigation of changes in the surface structure of $Li_xNi_{0.8}Co_{0.15}Al_{0.05}O_2$ cathode materials induced by the initial charge. *Chem. Mater.* **2014**, *26*, 1084–1092.

[20] Zheng, J. M.; Gu, M.; Xiao, J.; Zuo, P. J.; Wang, C. M.; Zhang, J. G. Corrosion/fragmentation of layered composite cathode and related capacity/voltage fading during cycling process. *Nano Lett.* **2013**, *13*, 3824–3830.

[21] Li, Q.; Li, G. S.; Fu, C. C.; Luo, D.; Fan, J. M.; Li, L. P. K^+-doped $Li_{1.2}Mn_{0.54}Co_{0.13}Ni_{0.13}O_2$: A novel cathode material with an enhanced cycling stability for lithium-ion batteries. *ACS Appl. Mater. Interfaces* **2014**, *6*, 10330–10341.

[22] Wang, D. W.; Xin, C.; Zhang, M. J.; Bai, J. M.; Zheng, J. X.; Kou, R. H.; Peter Ko, J. Y.; Huq, A.; Zhong, G. M.; Sun, C. J. et al. Intrinsic role of cationic substitution in tuning Li/Ni mixing in high-Ni layered oxides. *Chem. Mater.* **2019**, *31*, 2731–2740.

[23] Chen, J.; Deng, W. T.; Gao, X.; Yin, S. Y.; Yang, L.; Liu, H. Q.; Zou, G. Q.; Hou, H. S.; Ji, X. B. Demystifying the lattice oxygen redox in layered oxide cathode materials of lithium-ion batteries. *ACS Nano* **2021**, *15*, 6061–6104.

[24] House, R. A.; Marie, J. J.; Pérez-Osorio, M. A.; Rees, G. J.; Boivin, E.; Bruce, P. G. The role of O_2 in O-redox cathodes for Li-ion batteries. *Nat. Energy* **2021**, *6*, 781–789.

[25] Hou, X. Y.; Ohta, K.; Kimura, Y.; Tamenori, Y.; Tsuruta, K.; Amezawa, K.; Nakamura, T. Lattice oxygen instability in oxide-based intercalation cathodes: A case study of layered $LiNi_{1/3}Co_{1/3}Mn_{1/3}O_2$. *Adv. Energy Mater.* **2021**, *11*, 2101005.

[26] Zhang, S. S. Problems and their origins of Ni-rich layered oxide cathode materials. *Energy Storage Mater.* **2020**, *24*, 247–254.

[27] Assat, G.; Tarascon, J. M. Fundamental understanding and practical challenges of anionic redox activity in Li-ion batteries. *Nat. Energy* **2018**, *3*, 373–386.

[28] Zhuang, Z. C.; Li, Y.; Li, Y. H.; Huang, J. Z.; Wei, B.; Sun, R.; Ren, Y. J.; Ding, J.; Zhu, J. X.; Lang, Z. Q. et al. Atomically dispersed nonmagnetic electron traps improve oxygen reduction activity of perovskite oxides. *Energy Environ. Sci.* **2021**, *14*, 1016–1028.

[29] Jung, R.; Metzger, M.; Maglia, F.; Stinner, C.; Gasteiger, H. A. Chemical versus electrochemical electrolyte oxidation on NMC111, NMC622, NMC811, LNMO, and conductive carbon. *J. Phys. Chem. Lett.* **2017**, *8*, 4820–4825.

[30] Li, W. D.; Dolocan, A.; Oh, P.; Celio, H.; Park, S.; Cho, J.; Manthiram, A. Dynamic behaviour of interphases and its implication on high-energy-density cathode materials in lithium-ion batteries. *Nat. Commun.* **2017**, *8*, 14589.

[31] Sun, Y. K.; Chen, Z. H.; Noh, H. J.; Lee, D. J.; Jung, H. G.; Ren, Y.; Wang, S.; Yoon, C. S.; Myung, S. T.; Amine, K. Nanostructured high-energy cathode materials for advanced lithium batteries. *Nat. Mater.* **2012**, *11*, 942–947.

[32] Kim, J. M.; Zhang, X. H.; Zhang, J. G.; Manthiram, A.; Meng, Y. S.; Xu, W. A review on the stability and surface modification of layered transition-metal oxide cathodes. *Mater. Today* **2021**, *46*, 155–182.

[33] Weigel, T.; Schipper, F.; Erickson, E. M.; Susai, F. A.; Markovsky, B.; Aurbach, D. Structural and electrochemical aspects of $LiNi_{0.8}Co_{0.1}Mn_{0.1}O_2$ cathode materials doped by various cations. *ACS Energy Lett.* **2019**, *4*, 508–516.

[34] Alvarado, J.; Schroeder, M. A.; Zhang, M. H.; Borodin, O.; Gobrogge, E.; Olguin, M.; Ding, M. S.; Gobet, M.; Greenbaum, S.; Meng, Y. S. et al. A carbonate-free, sulfone-based electrolyte for high-voltage Li-ion batteries. *Mater. Today* **2018**, *21*, 341–353.

[35] Wang, Y.; Wang, D. S.; Li, Y. D. Rational design of single-atom site electrocatalysts: From theoretical understandings to practical applications. *Adv. Mater.* **2021**, *33*, 2008151.

[36] Meng, G.; Zhang, J.; Li, X. Y.; Wang, D. S.; Li, Y. D. Electronic structure regulations of single-atom site catalysts and their effects on the electrocatalytic performances. *Appl. Phys. Rev.* **2021**, *8*, 021321.

[37] Chen, S. H.; Wang, B. Q.; Zhu, J. X.; Wang, L. Q.; Ou, H. H.; Zhang, Z. D.; Liang, X.; Zheng, L. R.; Zhou, L.; Su, Y. Q. et al. Lewis acid site-promoted single-atomic Cu catalyzes electrochemical CO_2 methanation. *Nano Lett.* **2021**, *21*, 7325–7331.

[38] Jing, H. Y.; Zhu, P.; Zheng, X. B.; Zhang, Z. D.; Wang, D. S.; Li, Y. D. Theory-oriented screening and discovery of advanced energy transformation materials in electrocatalysis. *Adv. Powder Mater.*, in press, https://doi.org/10.1016/j.apmate.2021.10.004.

[39] Xie, H. B.; Du, K.; Hu, G. R.; Peng, Z. D.; Cao, Y. B. The role of sodium in $LiNi_{0.8}Co_{0.15}Al_{0.05}O_2$ cathode material and its electrochemical behaviors. *J. Phys. Chem. C* **2016**, *120*, 3235–3241.

[40] Xie, Q.; Li, W. D.; Manthiram, A. A Mg-doped high-nickel layered oxide cathode enabling safer, high-energy-density Li-ion batteries. *Chem. Mater.* **2019**, *31*, 938–946.

[41] Jeong, M.; Kim, H.; Lee, W.; Ahn, S. J.; Lee, E.; Yoon, W. S. Stabilizing effects of Al-doping on Ni-rich $LiNi_{0.80}Co_{0.15}Mn_{0.05}O_2$ cathode for Li rechargeable batteries. *J. Power Sources* **2020**, *474*, 228592.

[42] Mo, Y.; Guo, L. J.; Cao, B. K.; Wang, Y. G.; Zhang, L.; Jia, X. B.; Chen, Y. Correlating structural changes of the improved cyclability upon Nd-substitution in $LiNi_{0.5}Co_{0.2}Mn_{0.3}O_2$ cathode materials. *Energy Storage Mater.* **2019**, *18*, 260–268.

[43] Cui, Z. H.; Xie, Q.; Manthiram, A. Zinc-doped high-nickel, low-cobalt layered oxide cathodes for high-energy-density lithium-ion batteries. *ACS Appl. Mater. Interfaces* **2021**, *13*, 15324–15332.

[44] Ryu, H. H.; Park, G. T.; Yoon, C. S.; Sun, Y. K. Suppressing detrimental phase transitions via tungsten doping of $LiNiO_2$ cathode for next-generation lithium-ion batteries. *J. Mater. Chem. A* **2019**, *7*, 18580–18588.

[45] Huang, Y.; Liu, X.; Yu, R. Z.; Cao, S.; Pei, Y.; Luo, Z. G.; Zhao, Q. L.; Chang, B. B.; Wang, Y.; Wang, X. Y. Tellurium surface doping to enhance the structural stability and electrochemical performance of layered Ni-rich cathodes. *ACS Appl. Mater. Interfaces* **2019**, *11*, 40022–40033.

[46] Jamil, S.; Bin Yousaf, A.; Hee Yoon, S.; Suk Han, D.; Yang, L.; Kasak, P.; Wang, X. Y. Dual cationic modified high Ni-low co layered oxide cathode with a heteroepitaxial interface for high energy-density lithium-ion batteries. *Chem. Eng. J.* **2021**, *416*, 129118.

[47] Breuer, O.; Chakraborty, A.; Liu, J.; Kravchuk, T.; Burstein, L.; Grinblat, J.; Kauffman, Y.; Gladkih, A.; Nayak, P.; Tsubery, M. et al. Understanding the role of minor molybdenum doping in $LiNi_{0.5}Co_{0.2}Mn_{0.3}O_2$ electrodes: From structural and surface analyses and theoretical modeling to practical electrochemical cells. *ACS Appl. Mater. Interfaces* **2018**, *10*, 29608–29621.

[48] Shen, Y. B.; Wu, Y. Q.; Xue, H. J.; Wang, S. H.; Yin, D. M.; Wang, L. M.; Cheng, Y. Insight into the coprecipitation-controlled crystallization reaction for preparing lithium-layered oxide cathodes. *ACS Appl. Mater. Interfaces* **2021**, *13*, 717–726.

[49] Yang, H. P.; Wu, H. H.; Ge, M. Y.; Li, L. J.; Yuan, Y. F.; Yao, Q.; Chen, J.; Xia, L. F.; Zheng, J. M.; Chen, Z. Y. et al. Simultaneously dual modification of Ni-rich layered oxide cathode for high-energy lithium-ion batteries. *Adv. Funct. Mater.* **2019**, *29*, 1808825.

[50] Jia, G. F.; Li, F. Q.; Wang, J.; Liu, S. Q.; Yang, Y. L. Dual substitution strategy in Co-free layered cathode materials for superior lithium ion batteries. *ACS Appl. Mater. Interfaces* **2021**, *13*, 18733–18742.

[51] Sun, H. B.; Cao, Z. L.; Wang, T. R.; Lin, R.; Li, Y. Y.; Liu, X.; Zhang, L. L.; Lin, F.; Huang, Y. H.; Luo, W. Enabling high rate performance of Ni-rich layered oxide cathode by uniform titanium doping. *Mater. Today Energy* **2019**, *13*, 145–151.

[52] Shen, Y. B.; Xue, H. J.; Wang, S. H.; Wang, Z. M.; Zhang, D. Y.; Yin, D. M.; Wang, L. M.; Cheng, Y. A highly promising high-nickel low-cobalt lithium layered oxide cathode material for high-performance lithium-ion batteries. *J. Colloid Interface Sci.* **2021**, *597*, 334–344.

[53] Han, B.; Xu, S.; Zhao, S.; Lin, G. X.; Feng, Y. Z.; Chen, L. B.; Ivey, D. G.; Wang, P.; Wei, W. F. Enhancing the structural stability of Ni-rich layered oxide cathodes with a preformed Zr-concentrated defective nanolayer. *ACS Appl. Mater. Interfaces* **2018**, *10*, 39599–39607.

[54] Shen, Y. B.; Xue, H. J.; Wang, S. H.; Zhang, D. Y.; Yin, D. M.; Wang, L. M.; Cheng, Y. Ammonia-low coprecipitation synthesis of lithium layered oxide cathode material for high-performance battery. *Chem. Eng. J.* **2021**, *411*, 128487.

[55] Hong, C. Y.; Leng, Q. Y.; Zhu, J. P.; Zheng, S. Y.; He, H. J.; Li, Y. X.; Liu, R.; Wan, J. J.; Yang, Y. Revealing the correlation between structural evolution and Li^+ diffusion kinetics of nickel-rich cathode materials in Li-ion batteries. *J. Mater. Chem. A* **2020**, *8*, 8540–8547.

[56] Lee, W.; Muhammad, S.; Kim, T.; Kim, H.; Lee, E.; Jeong, M.; Son, S. H.; Ryou, J. H.; Yoon, W. S. New insight into Ni-rich layered structure for next-generation Li rechargeable batteries. *Adv. Energy Mater.* **2018**, *8*, 1701788.

[57] Li, J. Y.; Manthiram, A. A comprehensive analysis of the interphasial and structural evolution over long-term cycling of ultrahigh-nickel cathodes in lithium-ion batteries. *Adv. Energy Mater.* **2019**, *9*, 1902731.

[58] Wu, F.; Liu, N.; Chen, L.; Su, Y. F.; Tan, G. Q.; Bao, L. Y.; Zhang, Q. Y.; Lu, Y.; Wang, J.; Chen, S. et al. Improving the reversibility of the H2-H3 phase transitions for layered Ni-rich oxide cathode towards retarded structural transition and enhanced cycle stability. *Nano Energy* **2019**, *59*, 50–57.

[59] Xiao, Y. G.; Liu, T. C.; Liu, J. J.; He, L. H.; Chen, J.; Zhang, J. R.; Luo, P.; Lu, H. L.; Wang, R.; Zhu, W. M. et al. Insight into the origin of lithium/nickel ions exchange in layered $Li(Ni_xMn_yCo_z)O_2$ cathode materials. *Nano Energy* **2018**, *49*, 77–85.

[60] Zheng, J. X.; Ye, Y. K.; Liu, T. C.; Xiao, Y. G.; Wang, C. M.; Wang, F.; Pan, F. Ni/Li disordering in layered transition metal oxide: Electrochemical impact, origin, and control. *Acc. Chem. Res.* **2019**, *52*, 2201–2209.

[61] Wu, F. L.; Kim, G. T.; Kuenzel, M.; Zhang, H.; Asenbauer, J.; Geiger, D.; Kaiser, U.; Passerini, S. Elucidating the effect of iron doping on the electrochemical performance of cobalt-free lithium-rich layered cathode materials. *Adv. Energy Mater.* **2019**, *9*, 1902445.

[62] Mu, L. Q.; Lin, R. Q.; Xu, R.; Han, L. L.; Xia, S. H.; Sokaras, D.; Steiner, J. D.; Weng, T. C.; Nordlund, D.; Doeff, M. M. et al. Oxygen release induced chemomechanical breakdown of layered cathode materials. *Nano Lett.* **2018**, *18*, 3241–3249.